

Influence of heterogeneous refractivity on optical wave propagation in coastal environments

Ping He¹ · Christopher G. Nunalee¹ · Sukanta Basu¹ · Jean Minet² · Mikhail A. Vorontsov² · Steven T. Fiorino³

Received: 23 January 2015 / Accepted: 26 June 2015 / Published online: 15 July 2015
© Springer-Verlag Wien 2015

Abstract Spatial variations of refractivity significantly dictate the characteristics of optical wave propagation through the atmosphere. Consequently, the ability to simulate such propagation is highly dependent upon the accurate characterization of refractivity along the propagation path. Unfortunately, the scarcity of high spatiotemporal resolution observational data has forced many past studies of optical wave propagation to assume horizontally homogeneous (HH) atmospheric conditions. However, the (adverse) impact of such an assumption has not been quantified in the literature. In this paper, we attempt to fill this void by utilizing a mesoscale modeling-based approach to explicitly simulate atmospheric refraction. We then compare the differences of the HH refractivity fields to the mesoscale model-derived refractivity fields by means of a realistic atmospheric event and through ray tracing simulations. In this study, we model a coastal low-level jet, a common coastal atmospheric phenomenon which is associated with heterogeneous thermal and refractivity fields. Observational data from a radiosonde and a radar wind profiler near the northeastern region of the United States are used for model validation. The observed characteristics of low-level jet (e.g., evolution,

intensity, location) and associated temperature inversion are found to be reasonably well captured by the mesoscale model. The simulated nighttime refractivity gradient field manifests significant spatial heterogeneity; over land, the refractivity gradient is much stronger and amplified near the ground, whereas it becomes much weaker over the ocean. We quantify the effect of this heterogeneity on optical ray trajectories by simulating a suite of rays and documenting the variability of their altitudes at certain propagation ranges. It is found that the altitude of optical rays may vary tens of meters during a diurnal cycle, and at nighttime the rays may bend downward by more than 150 m at a range of 100 km. We run additional ray tracing simulations using refractivity profiles from a single location and assuming HH refractivity along the propagation path. It is observed that the HH approach yields instantaneous ray bending magnitudes up to 30 % less than the ray bending based on the refractivity simulated by the mesoscale model. At the same time, it is found that the mesoscale model-based refractivity fields may have uncertainty introduced by different factors associated with the model configuration. Of these factors, turbulence parameterization is explored in-depth and found to be responsible for more uncertainty than spatial grid resolution. To be more specific, different turbulence parameterizations are found to produce significantly varying temperature inversion parameters (e.g., height, magnitude), which are critical factors influencing ray trajectories. Collectively, these results highlight the potential advantages and disadvantages of utilizing a mesoscale model to simulate refractivity in coastal areas as opposed to assuming HH refractivity.

Communicated by R. Roebeling.

✉ Ping He
phe3@ncsu.edu

¹ Department of Marine, Earth, and Atmospheric Sciences, North Carolina State University, Raleigh, USA

² Intelligent Optics Laboratory, School of Engineering, University of Dayton, Dayton, USA

³ Department of Engineering Physics, Air Force Institute of Technology, Wright-Patterson Air Force Base, USA

Keywords Atmospheric refraction · Coastal low-level jet · Mesoscale modeling · Optical wave propagation · Turbulence parameterization

1 Introduction

The refractive index $n(\mathbf{r}, t)$, or refractivity ($N \equiv n - 1$), is the most important atmospheric variable that propagation of optical waves depends on (Andrews and Phillips 2005). Vertical gradient of refractivity, primarily attributed to the non-uniform temperature profile in the atmosphere, can greatly alter the trajectories of optical rays (known as ray bending). In practice, certain optical applications (e.g., communications, detections) can sometimes benefit from the bending of rays. For example, under super-refractive conditions, optical waves can propagate beyond the horizon, thereby extending the maximum target detection range (Dion 1995). However, the vertical variation of refractivity, and the resulting anomalous ray trajectories, can also induce adverse effects. Large ray bending can not only misrepresent the actual location of an object to an observer (Greenler 1980), but can also decrease the measured optical signal intensity (Doss-Hammel et al. 2004). In extreme conditions, severe ray bending can even generate optical phenomena such as wave ducting and mirage (Ghatak 2009). The ray bending behavior can be further complicated in the presence of horizontally heterogeneous refractivity, which can be prevalent in coastal environments (AGARD 1995).

The meteorological conditions harbored near coastal regions are extremely conducive to complex refractivity anomalies as a result of horizontal variability in surface features (e.g., land/sea surface temperature, aerodynamic roughness, energy budget). Phenomena such as coastal low-level jets (LLJs), land–sea breeze circulations, and coastal fronts are common due to the enhanced baroclinicity supplied by the land–sea interface (Hsu 1970; National Research Council 1992). In this study, we focus on the impact of heterogeneous refractivity induced by coastal LLJs on long-range optical wave propagations.

Quantification of the impact of realistic heterogeneous refraction, induced by mesoscale and synoptic scale phenomena, on optical wave propagation is a largely unexplored area of research. This is primarily attributed to the lack of information for the heterogeneous variation of atmospheric refractivity over long-range paths. An accurate modeling of electro-magnetic wave propagation requires high-resolution meteorological data to resolve the heterogeneous, time-dependent refractivity field. For example, in Dockery and Goldhirsh (1995), a horizontal spatial resolution of finer than 17 km was recommended for radio wave propagation. However, even in the United States, where dense meteorological networks/sensors are present, it is very hard to obtain observed meteorological data at this resolution. In less advanced regions of the world, meteorological information can be even more

scarce. One popular approach for circumventing the problem of sparse meteorological data is to assume horizontal homogeneity (HH approach) based on an observational profile from a single location (Goldhirsh and Dockery 1998). Of course in many locations, such as remote marine regions, even sparse profile datasets may not be available. In such situations, it is common to employ the Monin–Obukhov similarity theory (Monin and Obukhov 1954) to estimate the vertical profile of refractivity (MO approach) based on a single near-surface measurement, e.g., an ocean buoy (Dion et al. 2001; Doss-Hammel et al. 2002; Stein et al. 2003; Kunz et al. 2004; Dion et al. 2005). Neither the HH approach nor the MO approach considers heterogeneous refractivity induced by the mesoscale atmospheric structures. In addition, the Monin–Obukhov similarity theory is only valid within the surface layer, which can be very shallow (<10 m) under stably stratified conditions over land and ocean (Berström and Smedman 1995; Mahrt 2014). Therefore, the MO approach cannot be employed if optical waves propagate above the surface layer. These challenges highlight the need for high-fidelity atmospheric refractivity modeling (AGARD 1995).

Fortunately, advances in computing power have put mesoscale weather models in a position to accurately simulate and forecast atmospheric phenomena, ranging from one to thousands of kilometers in space and minutes to days in time (Orlanski 1975; Boybeyi 2000; Lin 2007). Mesoscale models have been proven to adequately resolve complex meteorological events such as convective clouds, thunderstorms, low-level jets, terrain-induced circulations, land–sea breezes, and gravity waves (Boybeyi 2000; Lin 2007). In contrast to relying completely on sparse observational data networks, the true benefit of using mesoscale simulations lies in their ability to provide time-dependent, three-dimensional fields of temperature, pressure, humidity, wind speed, and other meteorological variables (with temporal resolutions on the order of minutes and spatial resolution on the order of kilometers). Some of these variables can be used to diagnose the spatiotemporal variation of atmospheric refractivity for simulating or forecasting optical phenomena such as optical ducting and mirage formation. This technique has been adopted in a handful of research studies to document the influences of heterogeneous refractivity on propagation of radio wave (Burk and Thompson 1997; Atkinson et al. 2001; Haack et al. 2010; Wang et al. 2012). In our recent work (Nunalee et al. 2015), a coupled mesoscale modeling and ray tracing framework was utilized to investigate the impacts of anomalous refractivity, induced by the periodic shedding of island wake vortices, on long-range optical wave propagations.

Despite the benefits afforded by mesoscale models for analyses of optical wave propagation, there has been little evaluation of their uncertainty in simulating refraction. In some cases, these uncertainties may be high and often times sensitive to the particular flow being simulated (Wang et al. 2012). This paper concentrates on modeling of optical ray trajectories originating, and traveling through, the planetary boundary layer (PBL). The simulated flow structures and dynamics in the PBL are largely impacted by, and very sensitive to, the turbulence parameterization (i.e., PBL scheme, Nolan et al. 2009; Hu et al. 2010; Shin and Hong 2011; Xie et al. 2012; Nunalee and Basu 2013). Therefore, it is worth evaluating the impacts of various PBL schemes on the variations of refractivity, which consequently affect the optical wave propagation.

A synthesis of the above information provides the motivation for this paper which essentially documents some of the advantages and disadvantages of utilizing mesoscale models for predicting optical ray trajectories in the atmosphere. More specifically, this paper highlights the importance of capturing refractive heterogeneity induced by large-scale atmospheric structures while characterizing optical wave propagation in coastal regions. In addition, we comment on the uncertainty of mesoscale model-derived refraction diagnostics associated with turbulence parameterizations as well as grid resolution. To address these issues, we ran multiple mesoscale simulations of the northeastern coastal region of the United States. The simulated four-dimensional refractivity data were then used as input to a ray tracing code. This coupled modeling framework enabled us to study the properties of optical wave propagation within the coastal region along with the influences of an atmospheric phenomenon therein (i.e., LLJ). It is important to note that, in this study, we focus on kilometer-scale atmospheric refraction effects; the microscale effects associated with turbulence are not taken into account. Although the ray tracing cannot characterize the properties of optical wave propagation associated with turbulence, e.g., scintillation, beam wandering, it does depict beam centroid deviation from a straight line (ray bending) caused by non-uniform refractivity. It is therefore helpful in predicting optical phenomena such as optical ducting and mirage image formation, which can be utilized for detection and target tracking system from a practical standpoint (Kunz et al. 2002; Doss-Hammel et al. 2004).

The structure of this paper is as follows: Sect. 2 outlines the proposed framework of the coupled mesoscale and ray tracing simulation as well as the computational configurations. The mesoscale and the ray tracing simulation results are shown in Sect. 3 along with the PBL sensitivity analysis. Finally, in Sect. 4, conclusions and future directions are presented.

2 Data and method

In this study, we used the Weather Research and Forecasting (WRF) model (Skamarock et al. 2008), a state-of-the-art mesoscale model, to simulate a previously documented coastal LLJ event (Nunalee and Basu 2013). The time period selected for this study was July 15th–18th, 2011, during which a series of strong LLJs were observed along the New Jersey and New York coastline by a radar wind profiler in New Brunswick, NJ (RUTNJ) and a radiosonde in Upton, NY (OKX); see Fig. 1a for the corresponding locations. Data recorded by the RUTNJ profiler included wind speed and direction measurements for heights between ~ 100 and ~ 2000 m above ground level (AGL) with a temporal resolution of 10 minutes. On the other hand, the OKX radiosonde provided wind speed,

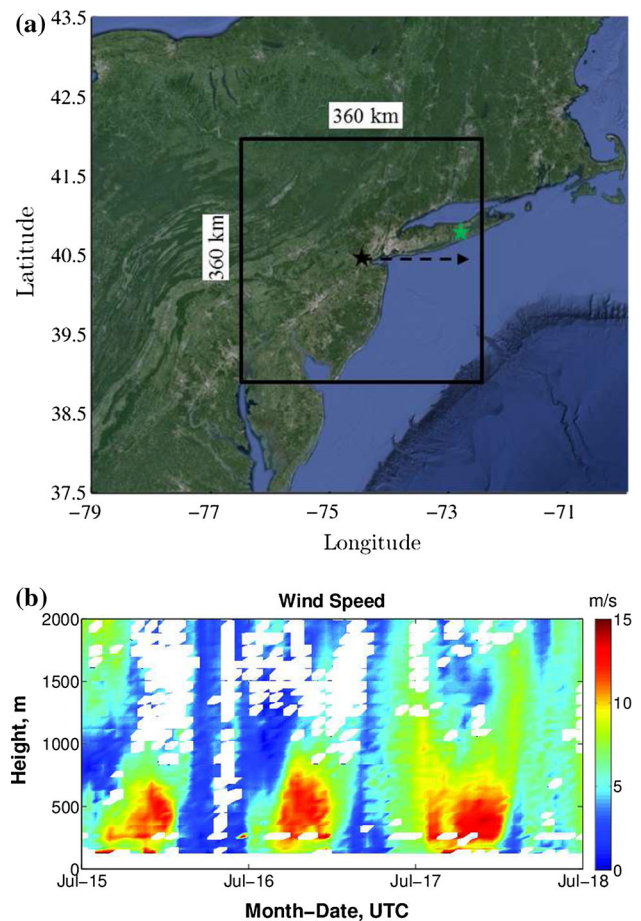


Fig. 1 **a** WRF model domain and observation site locations. Radar wind profiler location at RUTNJ (40.50 N / 74.45 W) (black star), and radiosonde launch site location at OKX (40.8694 N/72.8867 W) (green star). Black rectangle represents the innermost modeling domain (d03), and the black dash arrow is the wave propagation direction released from RUTNJ. **b** Low-level jets at RUTNJ during July 15th–18th, 2011. The time–height plot is based on the observational data from the radar wind profiler

temperature and humidity profiles twice daily (i.e., 00Z and 12Z). Low-level wind speed maxima and associated temperature inversions are clearly visible in these observational datasets. Figure 1b shows the time–height plot of measured wind speed at RUTNJ during July 15th–18th, 2011. During the three nights, the signatures of LLJs can be seen between 00UTC to 12UTC. The height and the intensity of the LLJs vary each day and the strongest wind speed can be found on July 17th. In Sect. 3, these observations will be used to validate the ability of the WRF model to capture vertical profiles of various meteorological variables associated with the LLJs.

Utilizing a two-dimensional ray tracing code in conjunction with the simulated refractivity fields from the WRF model (Nunalee et al. 2015), we study the influence of the LLJ on optical wave propagation in the northeastern coastal United States. Based on the dry and moist partial pressures of the air at a given grid cell (P_d and P_w , respectively) and temperature T , the refractivity N at wavelength λ is given by:

$$N = (n - 1) = \frac{A_d(\lambda)P_d + A_w(\lambda)P_w}{T}. \quad (1)$$

Here, the coefficients used for $A_d(\lambda)$ and $A_w(\lambda)$ are those put forth by Ciddor (1996). The ray tracing calculations were performed on a 2-D plane determined by the ray origin, the ray end, and the center of the earth. The refractivity fields extracted from the WRF model were then interpolated onto this 2-D plane for ray tracing simulations.

2.1 Mesoscale modeling

The WRF model, which was utilized to generate the mesoscale refractivity fields in this study, is a non-hydrostatic model which has been widely used in academia, government, and industry. Using the WRF preprocessing system (WPS), a nested numerical modeling domain with three nested levels (d01, d02, d03) was constructed (see location of d03 in Fig. 1a). The outermost (d01), intermediate (d02), and innermost (d03) domain sizes were 1782 km \times 1782 km, 1080 km \times 1080 km, and 360 km \times 360 km, respectively. The horizontal grid spacings for d01, d02, and d03 were 18, 6, and 2 km, respectively. The innermost domain was centered on the location of the RUTNJ radar wind profiler (40.50 N/74.45 W). In the vertical direction, each domain used the same grid structure of 51 grid points between \sim 8 m and \sim 16,000 m AGL. The density of vertical grid points in the atmospheric boundary layer was higher than that in the free atmosphere (i.e., 18 grid points below 1 km AGL) to provide a better representation of the detailed flow structure there. To evaluate the impact of WRF grid resolutions on ray tracing

simulation results, a grid resolution sensitivity study was conducted and reported in the “Appendix”.

Static land use and topography were obtained from the US Geological Survey and used as surface boundary conditions for the WRF simulations. The simulations were run for a total of 96 h (July 14th–18th, 2011) with the first 24 h being used for spin-up. The time steps for d01, d02, d03 were set at 90, 30, and 10 s, respectively. Our analyses in the following sections are based on output from d03 at 10-min intervals.

For initialization and boundary conditions, the ERA-Interim reanalysis dataset (Berrisford et al. 2009) was used. The ERA-Interim reanalysis dataset contains environmental data records from 1979 through the present at 6-h intervals and includes a horizontal resolution of approximately 79 km with 60 vertical coordinate levels.

Finally, the WRF model was run using physics parameterizations (with the exception of the PBL scheme) as reported in Nunalee and Basu (2013); Nunalee et al. (2014); Nunalee et al. (2015). In this study, the PBL scheme was varied to test model solution sensitivity. The sensitivity of the PBL scheme, above all other physics parameterizations, was studied due to its known influence on LLJ representation (Zhang et al. 2001; Storm et al. 2009; Nunalee and Basu 2013). In Sect. 3.3, we present results produced by running the WRF model multiple times using six different PBL schemes, while the other physical parameterizations were kept constant. The six PBL schemes evaluated here are: Yonsei University (YSU, Hong et al. 2006), Mellor-Yamada-Janjić (MYJ, Janjić 1994), Quasi-Normal Scale Elimination (QNSE, Sukoriansky et al. 2005), Mellor-Yamada Nakanishi and Niino Level 2.5 (MYNN2, Nakanishi and Niino 2006), Asymmetric Convective Model (ACM2, Pleim 2007a, b), and BouLac (BLc, Bougeault and Lacarrere 1989). In other sections, the YSU scheme is chosen as control case.

2.2 Ray tracing

Using the refractivity fields generated by the WRF model, ray tracing simulations were conducted. The ray trajectories were calculated by solving the Eikonal equations, or ray tracing equations:

$$\frac{d}{ds} \left(n \frac{dr_x}{ds} \right) = \frac{\partial n}{\partial x}, \quad (2)$$

$$\frac{d}{ds} \left(n \frac{dr_z}{ds} \right) = \frac{\partial n}{\partial z}, \quad (3)$$

where r_x and r_z are ray position in x (horizontal) and z (vertical) coordinate, s is the scalar distance along the ray path, and n is refractive index. Following Southwell (1982), Eqs. (2) and (3) were decomposed into a system of

first-order differential equations, and were numerically integrated along the propagation path. Please refer to Nunalee et al. (2015) for a detailed description of the ray tracing calculation.

A schematic of our ray tracing procedure is shown in Fig. 2. The ray origin was located at a certain height (h_o) above the ground, and the ray was released at an elevation angle (θ_i) with respect to the horizontal direction. The non-uniform refractivity in the atmosphere leads to a curved ray trajectory. The red solid point in Fig. 2 denotes the actual ray position $P_i(R_j)$ at range R_j . Owing to the ray bending, the apparent, unrefracted (representing propagation in a vacuum) ray position $P'_i(R_j)$ deviates vertically for a distance $\Delta_v = P'_i(R_j) - P_i(R_j)$. In super-refractive (stably stratified) conditions, the ray bends downward ($\Delta_v > 0$), whereas in sub-refractive (unstable) conditions, an upward bending ray trajectory can be observed which results in $\Delta_v < 0$. To an observer, the elevation and horizontal distance of a far-field object can be significantly misjudged in the case of large vertical deviation.

As shown in Fig. 1b, the heights of the observed coastal LLJs were generally between ~ 300 and ~ 500 m AGL. Therefore, we focused on optical wave propagations between the ray origin and two different ranges ($R_1 = 50$ km, $R_2 = 100$ km) and corresponding heights ($h_{1,2} = 400, 800$ m, respectively). Temporal variation of vertical deviation is investigated at these two ranges. The definitions of h_j and R_j can be seen in Fig. 2.

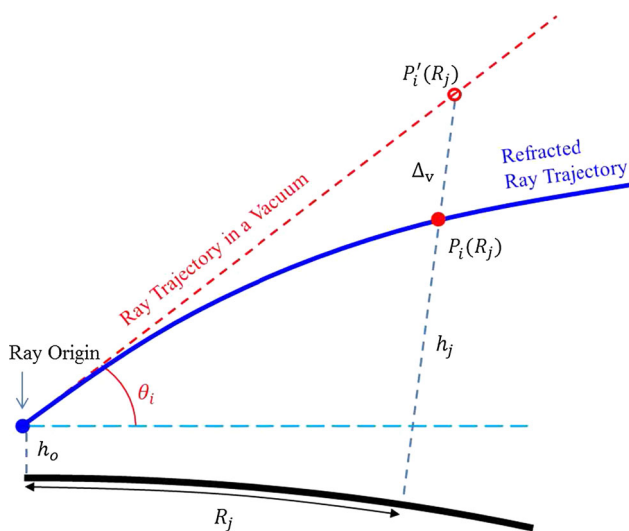


Fig. 2 Schematic of ray tracing (not to scale). Multiple rays were released from the ray origin at different elevation angles (θ_i), and the i th ray trajectory is shown as an illustration. The solid blue curve is the refracted ray trajectory in the atmosphere, while the red dashed line is the ray trajectory in the absence of an atmosphere (vacuum). The blue solid point denotes the ray origin. The red solid point, $P_i(R_j)$, represents the ray position at range R_j , while the red hollow point, $P'_i(R_j)$, is the apparent ray position

In this paper, the ray origin was located at RUTNJ, and 100 rays were released at a different elevation angle but with the same azimuth. The ray end was set at 150 km eastward from the ray origin as depicted in Fig. 1a. The wavelength studied here corresponded to near-infrared light at a wavelength of $\lambda = 1.55 \mu\text{m}$. The step size (δ) for all ray tracing calculations was selected to be 50 m which ensures numerical accuracy (Puchalski 1992). To prevent rays from reaching the surface, the observer height (h_o) was set at 80 m and the elevation angles θ_i ranged from -0.002 to $+0.010$ rad with 0.000 rad representing a perfectly horizontal ray at the origin.

2.3 Simplified diagnostic relationship for ray altitude calculation

In this subsection, a simplified relationship is presented for estimation of ray altitude at a given range. This diagnostic relationship is based on the following assumptions: the refractive index is close to unity ($n \approx 1$); $\frac{\partial n}{\partial z}$ is constant along the propagation path ($\frac{\partial n}{\partial z} = N_z$); the ray is released horizontally ($\frac{dr_z}{ds} = 0$ at $s = 0$); $r_z = 0$ at $s = 0$. Under these assumptions, we integrate Eq. (3) twice and obtain (Basu et al. 2015):

$$r_z = \frac{1}{2} N_z s^2, \tag{4}$$

Using this diagnostic expression, one can estimate the ray altitude at any given range (s) and refractivity gradient (N_z), or vice versa. A positive N_z will result in an upward bending of a ray ($r_z > 0$), while a negative N_z will induce a downward bending of a ray ($r_z < 0$). Please note that r_z is different from the ray altitude (h) due to the curvature of the earth, i.e., $h = r_z + h_c + h_0$. Here $h_0 = 80$ m is ray origin height, and h_c is the elevation of a horizontal ray due to the earth's curvature. For $s = 50$ and 100 km, $h_c \approx 196$ and 785 m, respectively.

3 Results and discussion

In this section, we present the mesoscale and ray tracing simulation results in detail. The spatiotemporal variations of wind speed and temperature are shown and compared with the observational data. Particular attention is given to the diurnal cycles of high refractivity gradients associated with the LLJs. The implications of these features on optical wave propagation are also highlighted wherever possible. Large nocturnal fluctuations in ray trajectories are quantified by ray altitude and vertical deviation metrics. Finally, the influence of the PBL schemes on the simulated refractivity and the associated ray tracing results is documented.

3.1 Simulated mesoscale meteorology

Figure 3 shows the wind speed contour at 350 m AGL for two different times. The high wind speed associated with the LLJ can be clearly seen around OKX and RUTNJ at nighttime (see Fig. 3a). The wind speed maxima during nighttime hours compared to the relatively lower daytime speeds (Fig. 3b) is a characteristic of LLJs. This diurnal wind speed pattern was also measured by the radar wind profiler at RUTNJ during July 15th–18th, 2011 (refer to Fig. 1b).

Vertical profiles of simulated wind speed, temperature, water vapor mixing ratio, and refractivity gradient at OKX are shown in Fig. 4 along with radiosonde observations. The results produced by different PBL schemes are shown here for comparison; however, more detailed PBL

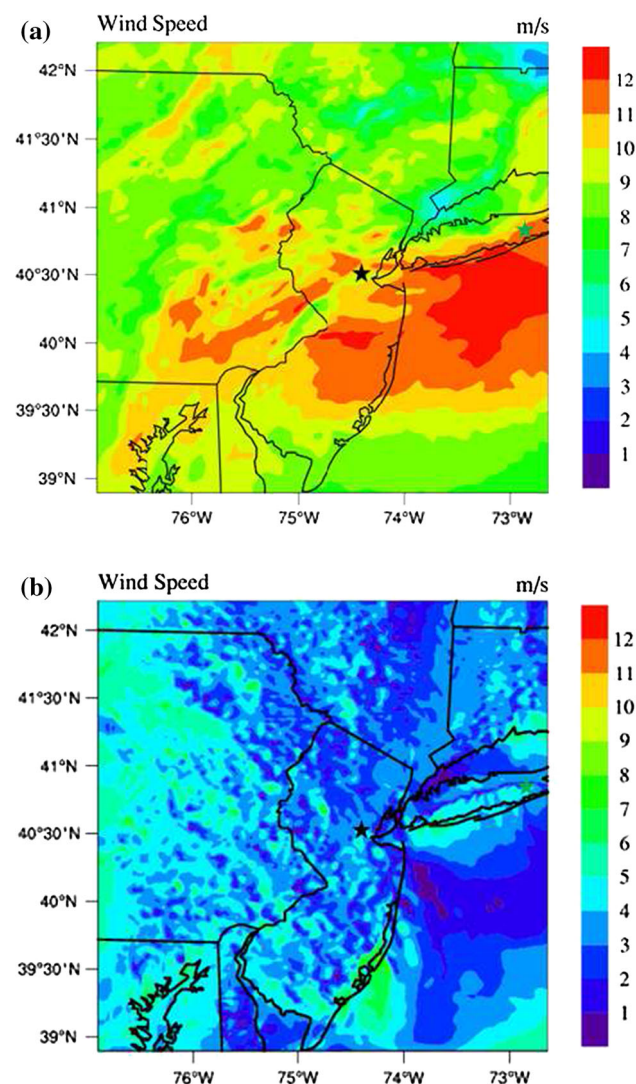


Fig. 3 Simulated wind speed contour at 350 m AGL: **a** 04UTC 07/17/2011, and **b** 18UTC 07/16/2011. The black and green stars represent the locations of RUTNJ and OKX, respectively

sensitivity experiments are documented in Sect. 3.3. Here, a sharp increase in wind speed at about 350 m AGL can be seen from the observational data (red dots) with a peak value of $\sim 12 \text{ m s}^{-1}$. The shape of the LLJ and the associated temperature inversion were more or less captured by the WRF model with the MYJ and QNSE schemes having relatively the best agreement with the observational data. However, all the PBL schemes overestimated temperature values under $\sim 250 \text{ m AGL}$.

The fact that most operational radiosondes are released twice per day limits their applicability to optical wave propagation studies. Manifestations of this limitation are further exacerbated when transient atmospheric phenomena (e.g., LLJ) are present. In these cases, mesoscale models are attractive as they enable analysis of the evolution of the refractivity field down to very short time scales. In Fig. 5, time–height plots of wind speed, temperature, potential temperature, and refractivity gradient at RUTNJ during July 15th–18th are shown. The diurnal cycles associated with the LLJs can be clearly seen from this figure. Nevertheless, a negative wind speed bias can be seen in Fig. 5a when comparing with the wind profiler observations (Fig. 1b), especially on July 15th and 16th. In addition, three prominent temperature inversions can be clearly seen below 500 m AGL during these nights. These sharp temperature gradients, which coincide with the LLJs, produced large negative refractivity gradients during 00UTC–12UTC. The sharpest refractivity gradient ($\frac{\partial n}{\partial z} \approx -5 \times 10^{-8} \text{ m}^{-1}$) occurred on the night of July 16th due to the relatively weaker shear-induced mixing. However, during the daytime, the boundary layer was well mixed and a much weaker refractivity gradient ($\frac{\partial n}{\partial z} \approx -2 \times 10^{-8} \text{ m}^{-1}$) was observed. The implications of these diurnal refractivity cycles on optical wave propagation are reported in Sect. 3.2.

3.2 Simulated optical wave propagation

The impingement of the simulated ray trajectories on the LLJ structures (see Figs. 1a, 3a) resulted in significant perturbations to individual ray trajectories. Instantaneous ray trajectories at two different times during July 15th–18th are shown in Fig. 6. The instantaneous refractivity gradient contours are overlaid on the plots for reference. For better visualization, only 50 ray trajectories are shown here. During daytime, there was no obvious high refractivity gradient at the wave propagation plane and the ray trajectories were evenly distributed (Fig. 6a). However, during the nighttime, the presence of the LLJ and the associated temperature inversion induced a band of high $\frac{\partial n}{\partial z}$. Over land (propagation distance $< 20 \text{ km}$), the high $\frac{\partial n}{\partial z}$ band concentrated near the ground ($< 200 \text{ m AGL}$). In contrast,

Fig. 4 Vertical profiles of variables at OKX, 12UTC 07/17/2011. The red dots are the observation data from the radiosonde, and the lines are the output of the WRF model with different PBL schemes: **a** wind speed, **b** temperature, **c** water vapor mixing ratio, and **d** vertical gradient of refractivity

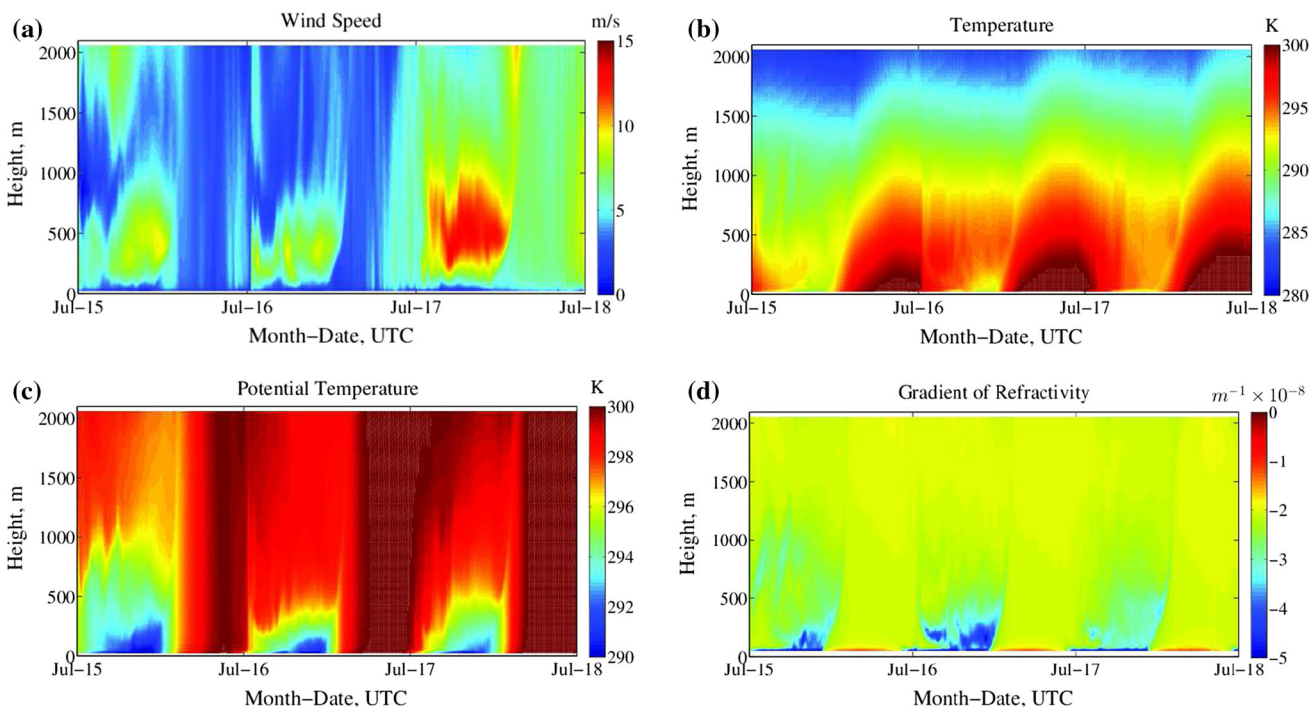
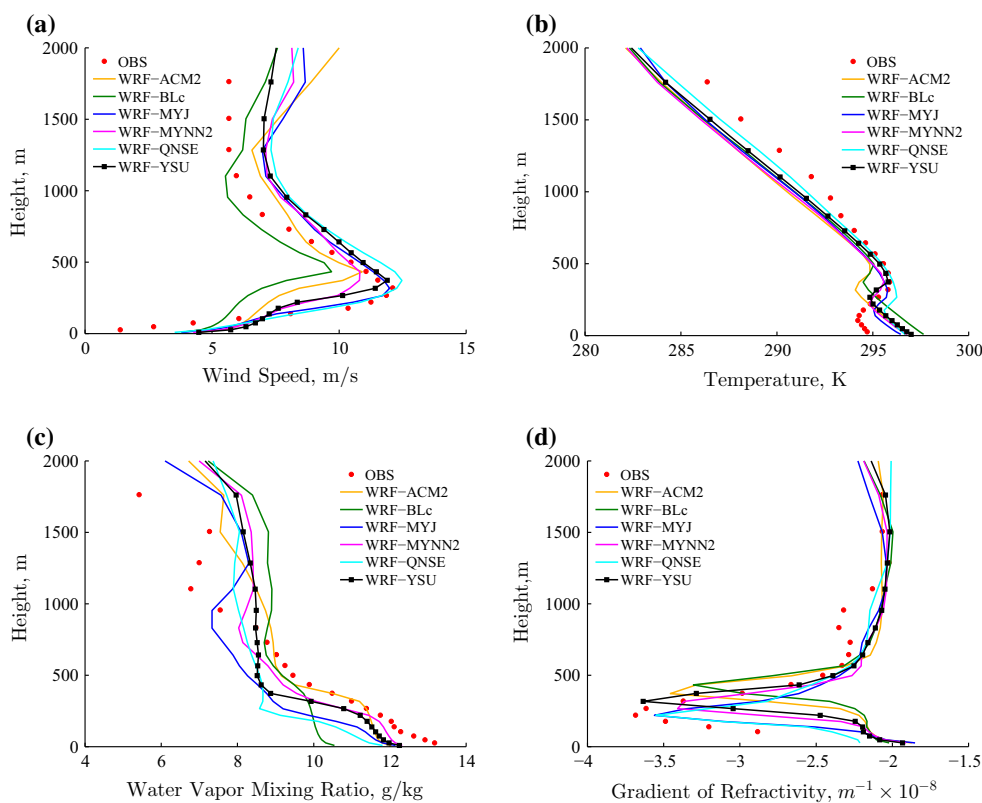


Fig. 5 Time–height plots of the simulated variables at RUTNJ during July 15th–18th, 2011: **a** wind speed, **b** temperature, **c** potential temperature, and **d** gradient of refractivity

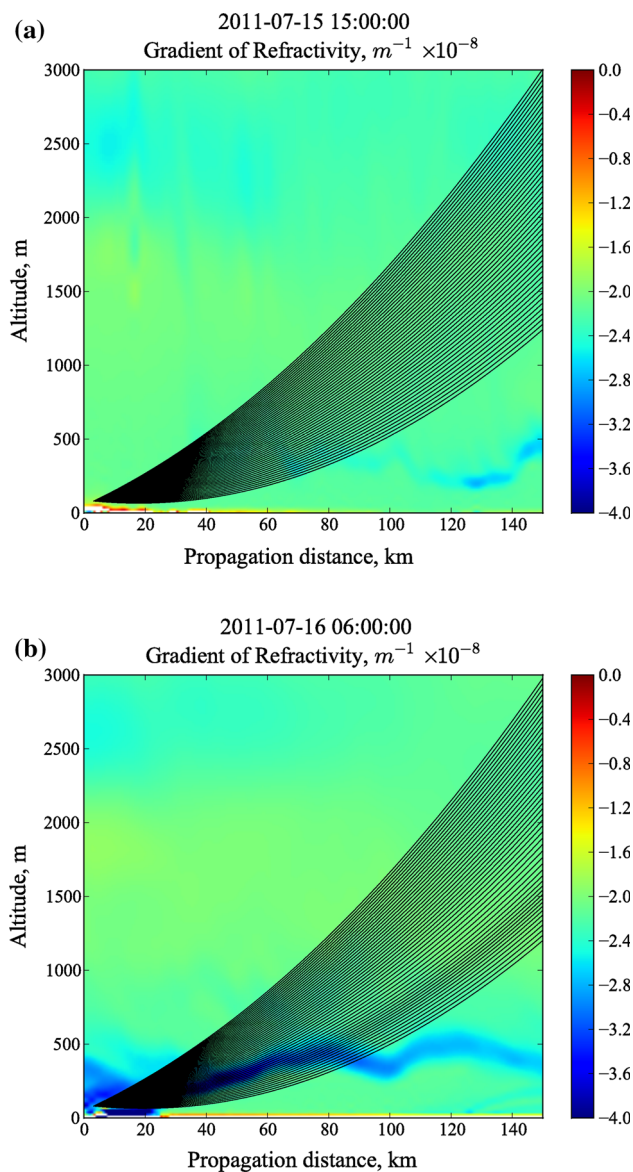


Fig. 6 Instantaneous ray trajectories at two different times during July 15th–18th. For better visualization, only 50 ray trajectories are shown. The rays are released from RUTNJ and the contours are the simulated gradient of refractivity: **a** 15UTC, 07/15/2011, and **b** 06UTC, 07/16/2011

over the ocean, the band became weaker and was elevated to about 500 m AGL. This high $\frac{\partial n}{\partial z}$ band caused anomalous ray trajectories and significant ray bending, as can be seen in Fig. 6b.

From the ray trajectories depicted in Fig. 6, we select the ray that is the most parallel to the surface at the observer location to monitor the temporal variations of its altitude at specific ranges. In addition, we investigate the differences that can be found using three different methods to compute ray trajectories: 4D, HH, and US1976. For 4D, we use the four-dimensional refractivity field

$N(x, y, z, t)$ obtained from the WRF output, where t is time, and x, y, z are latitude, longitude, and altitude coordinates, respectively. For HH, the refractivity field is chosen to be the vertical profile located in the middle of the wave propagation path, and horizontal homogeneity is assumed. For US1976, the refractivity field is purely one dimensional and the refractivity profile is calculated based on the modified US 1976 standard atmosphere (van der Werf 2003).

Time series of ray altitude with respect to different ranges (R) during July 15th–18th, 2011 are shown in Fig. 7a, b. It can be seen that the diurnal cycle of high $\frac{\partial n}{\partial z}$ produced large fluctuations over time for 4D. Due to the LLJ and the associated temperature inversion, super-refraction conditions formed at the top of the boundary layer at night and the ray bent downward significantly compared to daytime. For example, at $R = 100$ km, the ray altitude was 694 m at 08UTC July 16, corresponding to a ray bending of -171 m in the vertical direction; however, at 19UTC July 15, the ray altitude was 749 m with a ray bending of -116 m. At a relatively shorter range ($R = 50$ km), the ray altitude was approximately 247 m (-29 m bending) at 19UTC July 15 and 229 m (-47 m bending) at 08UTC July 16.

Utilizing the simulated ray altitude at $R = 50$ km in conjunction with the diagnostic relationship in Eq. (4), one can calculate an averaged refractivity gradient (N_z) along the ray propagation path, i.e., $N_z^{\text{day}} \approx -2.3 \times 10^{-8} \text{ m}^{-1}$ and $N_z^{\text{night}} \approx -3.8 \times 10^{-8} \text{ m}^{-1}$. The comparison between these diagnosed refractivity gradients and those explicitly simulated by the WRF model can be seen in Fig. 8. During the daytime, the WRF-based refractivity gradient was nearly constant due to strong mixing, and the diagnosed N_z^{day} qualitatively agreed with those values. This indicates that the traditional assumption of homogeneous refractivity can be valid in the daytime convective boundary layer due to the relatively weak thermal heterogeneity. However, during the nighttime, significant differences were observed. The ray passed through the inversion layer at $R \approx 20$ and 60 km, where two $\frac{\partial n}{\partial z}$ (negative) peaks can be clearly observed. At $R \approx 20$ km, the $\frac{\partial n}{\partial z}$ simulated by WRF ($\approx -4.8 \times 10^{-8} \text{ m}^{-1}$) was much higher than the diagnosed N_z^{night} . The ray altitude increased along the ray path and $\frac{\partial n}{\partial z}$ decreased drastically, especially above the boundary layer where the inversion-induced high $\frac{\partial n}{\partial z}$ is absent.

The above results indicate that the assumption of homogeneous refractivity fields can introduce significant error to the simulated ray trajectories, especially at nighttime. For example, if one utilizes the refractivity gradient in the middle of the propagation path (over the ocean), i.e., the HH approach, the diurnal fluctuation of the simulated

Fig. 7 Time series of the simulated ray altitude and vertical deviation at different ranges (R) and heights (h) during July 15th–18th, 2011: **a** ray altitude, $R = 50$ km, **b** ray altitude, $R = 100$ km, **c** vertical deviation, $R = 50$ km, $h = 400$ m, **d** vertical deviation, $R = 100$ km, $h = 800$ m

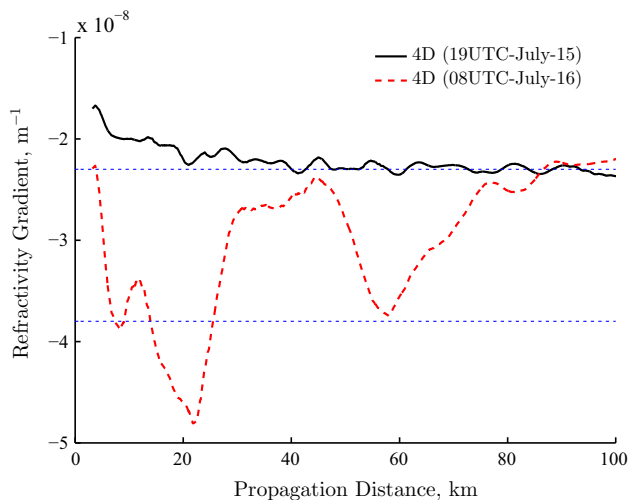
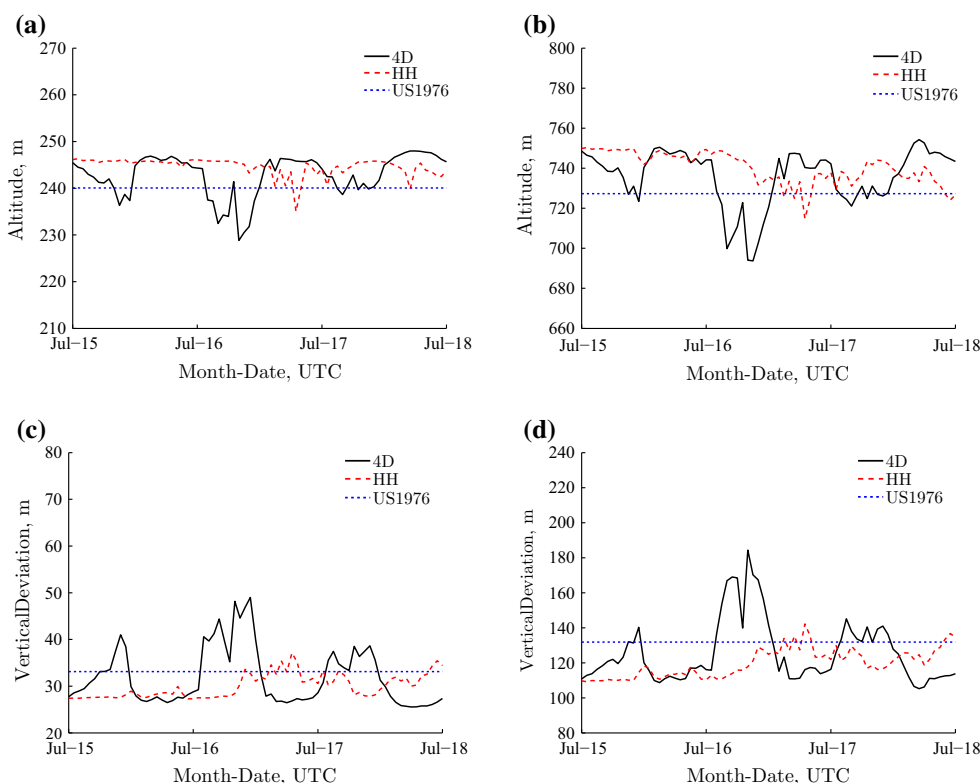


Fig. 8 Simulated refractivity gradient along the ray path (4D). The blue dotted lines denote the diagnosed refractivity gradient (-2.3×10^{-8} and $-3.8 \times 10^{-8} \text{ m}^{-1}$ for 19UTC July 15 and 08UTC July 16, respectively) using the diagnostic relationship in Eq. (4)

ray altitude becomes much less significant (Fig. 7). That is, the maximum differences between 4D and HH are 16 and 48 m for $R = 50$ and 100 km, respectively. This is primarily attributed to the fact that the diurnal cycle over the ocean is much less prominent than over land. As a result, the refractivity profile in the middle of the ray path is hardly

affected by the temperature inversion and $\frac{\partial n}{\partial z}$ varies little during the three nights. It is also important to note that, for the HH approach, the simulated ray trajectories can be very different if one chooses another location to obtain the refractivity profile; this dependency is another drawback of the HH approach. Meanwhile, it is needless to point out that the result obtained from the non-site-specific, time-invariant profile of US1976 is unable to capture the diurnal cycles associated with the LLJ. The maximal differences of the simulated ray altitudes between US1976 and 4D are approximately 12 and 34 m for $R = 50$ and 100 km, respectively. These results highlight the potential advantages of a mesoscale modeling approach to ray tracing.

Next, we analyzed the temporal variability of ray bending through the vertical deviation metric, which quantifies the vertical distance between an actual and an apparent ray position (Fig. 2). Time series of vertical deviation at different ranges and heights during July 15th–18th are shown in Fig. 7c, d. Super-refraction conditions are evident during the nighttime hours (00UTC–12UTC) as the vertical deviation increases sharply with the highest deviation observed on July 16th. The maximum difference of vertical deviation between night and day is about 23 and 79 m for $R = 50$ and 100 km, respectively. Profiles of vertical deviation at two different ranges are shown in Fig. 9. One can see that, during the night (06UTC), the vertical deviation was much larger at all altitudes than it

was during the day (15UTC). In addition, the change in vertical deviation with increasing altitude was much more pronounced during the nighttime compared to the daytime. This was due to the defined LLJ signature which was associated with a sharp peak in vertical deviation at about 300 and 800 m for $R = 50$ and 100 km, respectively. Again, refractivity models assuming horizontal homogeneity lack the ability to represent complex features such as these (Fig. 7c, d).

3.3 Sensitivity to the turbulence parameterizations

The WRF model provides several built-in PBL parameterization options. These PBL schemes are formulated using different underlying assumptions, e.g., local or non-local transport (Stensrud 2007). As can be seen in Fig. 4, the PBL schemes can have substantial impacts on

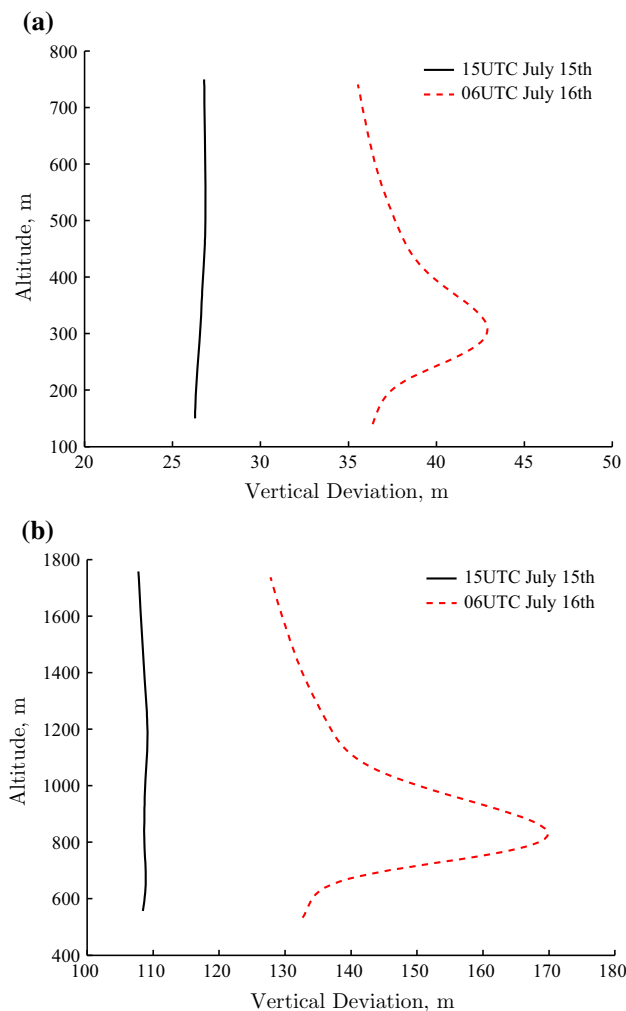


Fig. 9 Profiles of the simulated vertical deviation with respect to altitude at two different ranges: **a** $R = 50$ km, and **b** $R = 100$ km

simulation results and consequently the simulated optical wave propagation. An in-depth PBL scheme sensitivity study is discussed in this section. Here, we considered six different PBL schemes (ACM2, BLc, MYJ, MYNN2, QNSE, and YSU).

Time–height plots of refractivity with different PBL schemes at RUTNJ during July 15th–18th, 2011 are shown in Fig. 10. Although all the PBL schemes simulate similar diurnal cycles of refractivity gradient, the magnitudes differ, especially during the nighttime. Overall, the QNSE scheme simulated the highest magnitude of refractivity gradient during the three nights while the magnitude predicted by the BLc scheme was the lowest. This poor prediction of the BLc scheme is probably attributed to its nighttime overmixing characteristic (Bravo et al. 2008). Meanwhile, the control PBL scheme (YSU) presented a moderate refractivity gradient prediction. Vertical profiles of the simulated refractivity gradient are shown in Fig. 11. The sharp increase of refractivity gradient was simulated by all of the PBL schemes; however, the maximal difference of simulated refractivity gradient was approximately $\pm 25\%$ with respect to the ensemble mean value between different PBL schemes at ~ 350 m AGL. The averaged difference in the lowest 2000 m AGL was about $\pm 8\%$. In addition to the magnitude, the vertical location of the sharp $\frac{\partial n}{\partial z}$ varied; for example, it was located at 260 and 370 m for the QNSE scheme and the BLc scheme, respectively. This is primarily due to the different predictions of PBL heights by these PBL schemes. As documented below, the difference in the predicted magnitude and location of the high $\frac{\partial n}{\partial z}$ induce significant uncertainty to the simulated ray trajectories.

The evolution of ray altitude over time with respect to different PBL schemes at a range $R = 50$ km is shown in Fig. 12a. One can see that, due to the different predicted refractivity gradient, the altitude variations with respect to different PBL schemes were most significant on July 16th. The altitude simulated by the QNSE scheme was ~ 34 m lower than that simulated by the BLc scheme. The maximal and averaged differences of simulated ray altitude between various PBL schemes are about $\pm 8\%$ and $\pm 2\%$, respectively. According to the diagnostic relationship in Eq. (4), a 34-m difference in ray altitude corresponds to a difference of $\sim 2.7 \times 10^{-8} \text{ m}^{-1}$ in N_z . Note that this value is much larger than the $\frac{\partial n}{\partial z}$ difference between the QNSE and the BLc schemes observed in Fig. 11. This is primarily owing to the fact that the predicted vertical location of the high $\frac{\partial n}{\partial z}$ for the QNSE scheme is much lower than the BLc scheme. Since the optical rays originated near the ground, the sharp increase in $\frac{\partial n}{\partial z}$ closer to the ground is expected to have greater impacts on the ray trajectory. In other words, both

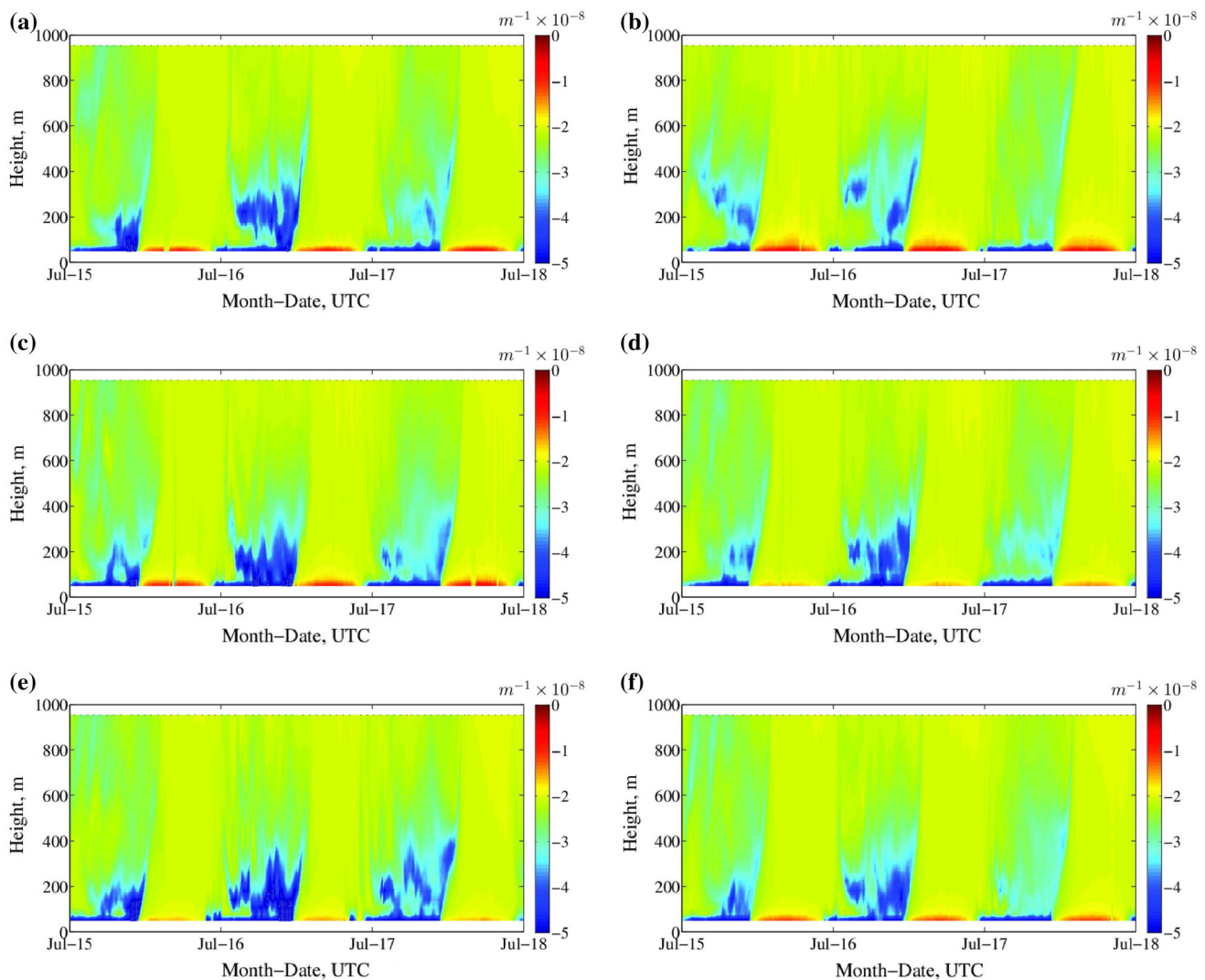


Fig. 10 Time–height plots of simulated refractivity gradient with different PBL schemes at RUTNJ during July 15th–18th, 2011: **a** ACM2, **b** BLc, **c** MYJ, **d** MYNN2, **e** QNSE, and **f** YSU

magnitude and vertical location of the high $\frac{\partial n}{\partial z}$ impact the simulated ray trajectories. The evolution of vertical deviations over time with respect to different PBL schemes at a range and height of $R = 50$ km and $h = 400$ m is shown in Fig. 12b. Compared to the variability of altitude, the absolute value for the vertical deviation variability was relatively low. The maximum difference of vertical deviation between the six PBL schemes being about 24 m in the night of July 16th. There are approximately $\pm 24\%$ (maximal) and $\pm 8\%$ (averaged) differences of simulated vertical deviation between different PBL schemes.

Based on the above results, it is evident that the coupled mesoscale modeling and ray tracing simulation framework is quite sensitive to physical parameterizations. In this study, we have evaluated the impact of the turbulence parameterization, i.e., PBL scheme, on the simulated ray trajectories and the uncertainty is shown to

be significant (much larger than the uncertainty induced by grid resolutions, please compare Figs. 12 with 13 in the “Appendix”). It is reasonable to expect that other physical parameterizations may also have noticeable impacts. For example, it was reported in Steeneveld et al. (2008) that the simulated LLJ and inversion structure in the stable boundary layer are sensitive to radiation schemes. Given the omnipresence of modeling errors and uncertainties, we recommended that multiphysics ensemble modeling framework (Tapiador et al. 2012; Kieu et al. 2014) be adopted. Under this framework, several mesoscale simulations are run using various physical parameterizations, e.g., turbulence, radiation, surface schemes. Based on the model output, one could synthesize a weighted ensemble prediction (Raftery et al. 2005), as well as quantify its uncertainty, for atmospheric refractivity estimation.

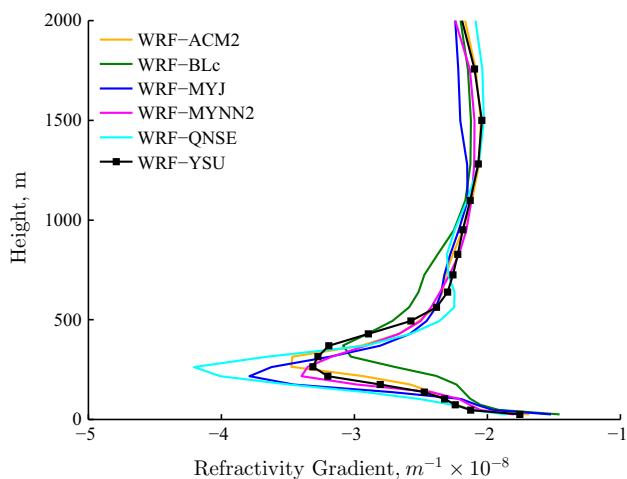


Fig. 11 Vertical profiles of the simulated refractivity gradient with different PBL schemes at RUTNJ (12UTC, 07/17/2011)

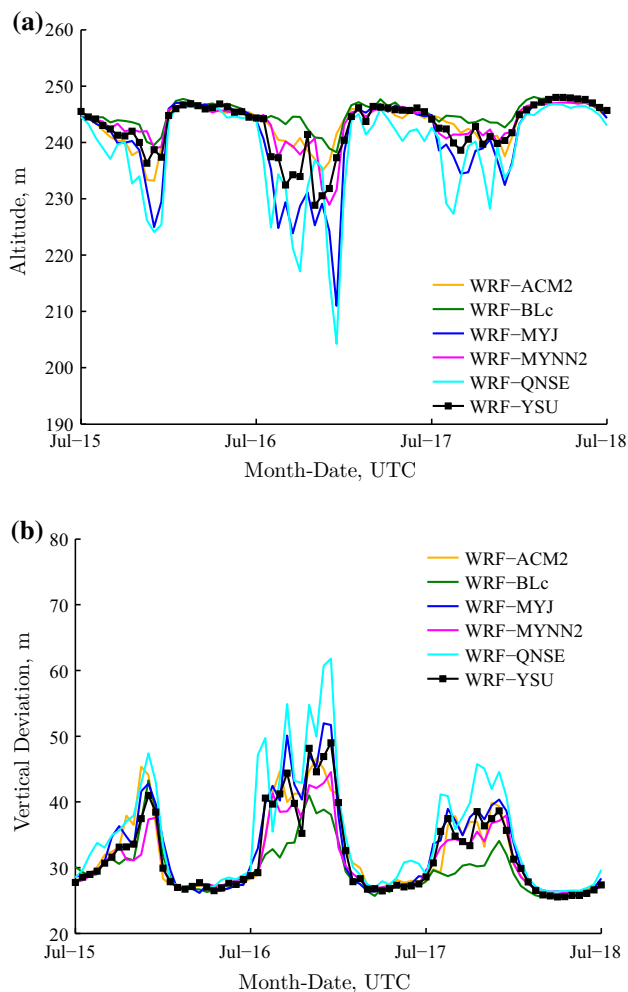


Fig. 12 Time series of the simulated ray altitude and vertical deviation with different PBL schemes: **a** ray altitude, $R = 50$ km, and **b** vertical deviation, $R = 50$ km, $h = 400$ m

4 Concluding remarks

In this paper, we simulated optical wave propagation in the northeastern coastal region of the United States during July 15th–18th, 2011. The simulations used realistic, heterogeneous refractivity fields generated by the WRF model which captured coastal low-level jets. The temperature inversions associated with the nocturnal LLJs induced sharp gradients of refractivity at the top of the atmospheric boundary layer (~ 350 m AGL).

Ray tracing simulations were then performed based on the refractivity fields generated by the WRF model. Anomalous ray trajectories were found during the nighttime hours as a result of the temperature inversion perturbations associated with the LLJs. The difference between the results produced by the mesoscale modeling approach and those produced using horizontally homogeneous refractivity profiles (HH approach) were significant. For a range of 100 km, the maximum differences of ray altitude and vertical deviation were about 48 and 75 m, respectively.

The above findings highlight the value of using mesoscale models to capture the dynamical features of atmospheric refractivity in coastal environments for long-range optical wave propagation. At the same time, we observed that the WRF model simulated refractivity and ensuing ray trajectories exhibited noteworthy sensitivity to turbulence parameterizations. For example, the maximal differences of simulated ray altitude and vertical deviation with respect to the ensemble mean value were approximately ± 8 and $\pm 24\%$, respectively, for a range of 50 km. These results highlight the need for a multiphysics ensemble modeling framework.

In addition, future efforts should be devoted to understanding the potential role of coupled mesoscale atmospheric–oceanic simulations on the characterization of low-altitude refractivity and optical wave propagation down to, and within, the surface layer. Moreover, additional coupled mesoscale–ray tracing simulations should be carried out to explore diverse atmospheric phenomena. These studies should aim to illustrate potential relationships between individual phenomena and optical metrics such as ray altitude displacement and vertical deviation. Lastly, it is essential that the accuracy of these modeling trials is verified by thorough comparison with observational data sources.

Acknowledgments The authors acknowledge financial support received from the Department of Defense (AFOSR grant under award number FA9550-12-1-0449) and the National Science Foundation (Grant AGS-1122315). Any opinions, findings and conclusions or recommendations expressed in this material are those of the authors and do not necessarily reflect the views of the Department of Defense or the National Science Foundation. The authors also acknowledge the use of computational resources at the NCSU's ARC cluster,

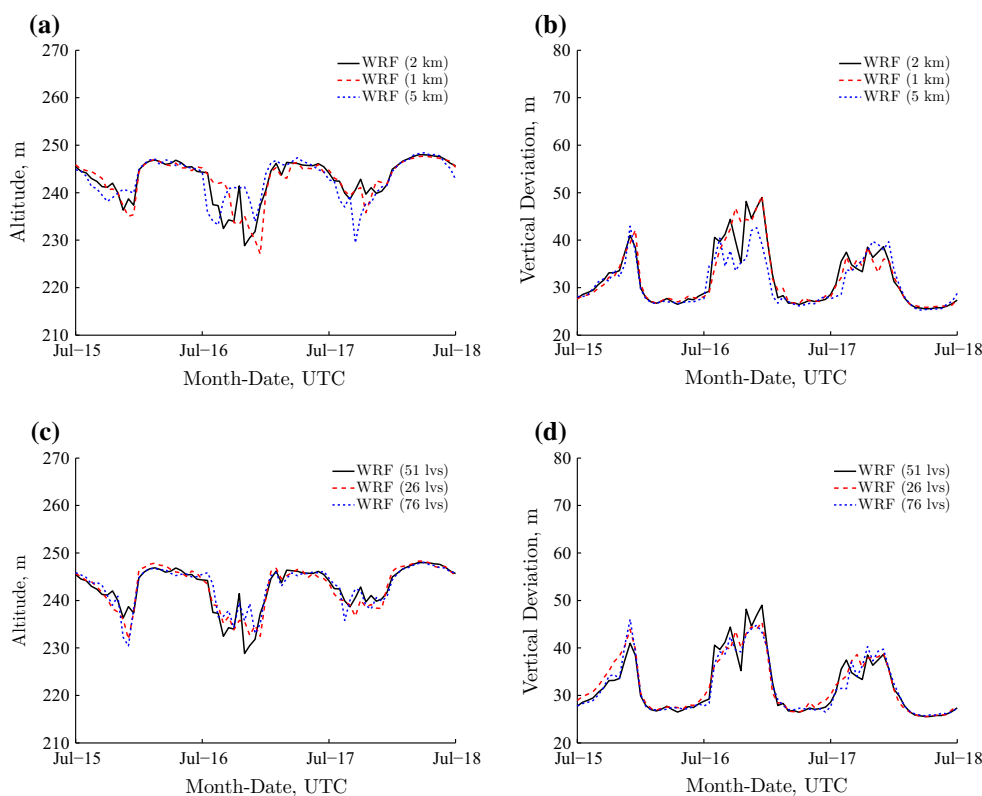
supported by the National Science Foundation (Grant 0958311). Finally, the authors thank Adam DeMarco for his valuable comments and suggestions to improve the quality of the paper.

Appendix: Sensitivity to grid resolution

In this appendix, we evaluate the sensitivity of grid spacing on the ray tracing simulation results. Figure 13 shows the time series of ray altitude and vertical deviation with different grid resolutions. The impacts of horizontal and vertical grid resolutions on the ray tracing simulation results are evaluated separately. For Fig. 13a, b, 51 vertical grids were used for all three horizontal grid spacings (i.e., 1, 2, and 5 km for the d03 domain, and the grid spacing

ratio between the nesting domains was kept to be 3). For Fig. 13c, d, the horizontal grid spacing was kept to be 2 km (d03 domain), and three vertical resolutions were adopted (i.e., 26, 51, and 76 vertical grid levels). Note that the control grid spacing configuration used in this paper is 2 km in the horizontal direction and 51 grids in the vertical direction (solid line in Fig. 13). One can see that, with further increasing the horizontal (i.e., 1 km) and vertical (i.e., 76 levels) resolutions, the changes in the ray tracing simulation results are relatively small. However, with a coarse grid resolution, noticeable discrepancies can be observed, especially for the 5 km horizontal grid spacing cases (Fig. 13a, b). Nevertheless, the grid resolutions have relatively less impact on the ray tracing results compared to the PBL schemes.

Fig. 13 Time series of the simulated ray altitude and vertical deviation with different grid resolutions ($R = 50$ km): **a** ray altitude and **b** vertical deviation with different horizontal resolutions, and **c** ray altitude and **d** vertical deviation with different vertical resolutions



References

- AGARD (1995) AGARD conference proceedings 576. SPIE press, propagation assessment in coastal environments
- Andrews LC, Phillips RL (2005) Laser beam propagation through random media, vol 152. SPIE press, Bellingham
- Atkinson BW, Li JG, Plant RS (2001) Numerical modeling of the propagation environment in the atmospheric boundary layer over the Persian Gulf. *J Appl Meteor* 40(3):586–603
- Basu S, McCrae J, Pollock Z, He P, Nunalee C, Basu S, Voelz DG, Fiorino S (2015) Comparison of atmospheric refractive index gradient variations derived from time-lapse imagery and mesoscale modeling. In: Propagation through and characterization of distributed volume turbulence and atmospheric phenomena, Optical Society of America, pp PM1C-4
- Berrisford P, Dee D, Fielding K, Fuentes M, Kallberg P, Kobayashi S, Uppala S et al (2009) The ERA-interim archive. *ERA Rep Ser* 1:1–16
- Berström H, Smedman AS (1995) Stably stratified flow in a marine atmospheric surface layer. *Bound Layer Meteor* 72(3):239–265
- Bougeault P, Lacarrere P (1989) Parameterization of orography-induced turbulence in a mesobeta-scale model. *Mon Wea Rev* 117(8):1872–1890
- Boybeyi Z (2000) A brief overview of mesoscale atmospheric features. In: Boybeyi Z (ed) Mesoscale atmospheric dispersion. WIT Press, pp 1–26
- Bravo M, Mira T, Soler M, Cuxart J (2008) Intercomparison and evaluation of MM5 and Meso-NH mesoscale models in the stable boundary layer. *Bound Layer Meteor* 128(1):77–101
- Burk SD, Thompson WT (1997) Mesoscale modeling of summertime refractive conditions in the Southern California Bight. *J Appl Meteor* 36(1):22–31
- Ciddor PE (1996) Refractive index of air: new equations for the visible and near infrared. *Appl Opt* 35(9):1566–1573
- Dion D (1995) Refraction effects on EO system detection ranges in coastal environments. In: AGARD conference proceedings 576, propagation assessment in coastal environments, p 9
- Dion D, Gardenal L, Lahaie P, Forand JL (2001) Calculation and simulation of atmospheric refraction effects in maritime environments. In: Proceedings of SPIE, vol 4167, pp 1–9
- Dion D, Seiffer D, Stein K, Forand L, Potvin G (2005) Raypath deviation under stable and unstable conditions. In: Proceedings of SPIE, vol 5981, p 598109
- Dockery GD, Goldhirsh J (1995) Atmospheric data resolution requirements for propagation assessment: case studies of range-dependent coastal environments. In: AGARD conference proceedings 576, propagation assessment in coastal environments, p 13
- Doss-Hammel SM, Zeisse CR, Barrios AE, de Leeuw G, Moerman M, de Jong AN, Frederickson PA, Davidson KL (2002) Low-altitude infrared propagation in a coastal zone: refraction and scattering. *Appl Opt* 41(18):3706–3724
- Doss-Hammel SM, Tsintikidis D, van Eijk A, Kunz G (2004) Refractive effects, turbulence, and the EOSTAR model. In: Proceedings of SPIE, vol 5406, pp 733–742
- Ghatak A (2009) Fermat's principle and its applications. In: Optics, Tata McGraw-Hill Publishing Company Limited
- Goldhirsh J, Dockery D (1998) Propagation factor errors due to the assumption of lateral homogeneity. *Radio Sci* 33(2):239–249
- Greenler R (1980) Rainbows, halos, and glories. Cambridge University Press, Cambridge
- Haack T, Wang C, Garrett S, Glazer A, Mailhot J, Marshall R (2010) Mesoscale modeling of boundary layer refractivity and atmospheric ducting. *J Appl Meteor Climatol* 49(12):2437–2457
- Hong SY, Noh Y, Dudhia J (2006) A new vertical diffusion package with an explicit treatment of entrainment processes. *Mon Wea Rev* 134(9):2318–2341
- Hsu SA (1970) Coastal air-circulation system: observations and empirical model. *Mon Wea Rev* 98(7):487–509
- Hu XM, Nielsen-Gammon JW, Zhang F (2010) Evaluation of three planetary boundary layer schemes in the WRF model. *J Appl Meteor Climatol* 49(9):1831–1844
- Janjić ZI (1994) The step-mountain eta coordinate model: further developments of the convection, viscous sublayer, and turbulence closure schemes. *Mon Wea Rev* 122(5):927–945
- Kieu C, Minh PT, Mai HT (2014) An application of the multi-physics ensemble Kalman filter to typhoon forecast. *Pure Appl Geophys* 171(7):1473–1497
- Kunz GJ, Moerman MM, Van Eijk AM (2002) ARTEAM: advanced ray tracing with earth atmospheric models. In: Proceedings of SPIE 4718, targets and backgrounds VIII: characterization and representation, pp 397–404
- Kunz GJ, Moerman MM, van Eijk AMJ, Doss-Hammel SM, Tsintikidis D (2004) EOSTAR: an electro-optical sensor performance model for predicting atmospheric refraction, turbulence, and transmission in the marine surface layer. In: Proceedings of SPIE, vol 5237, pp 81–92
- Lin YL (2007) Mesoscale dynamics. Cambridge University Press, Cambridge
- Mahrt L (2014) Stably stratified atmospheric boundary layers. *Annu Rev Fluid Mech* 46:23–45
- Monin AS, Obukhov AM (1954) Basic laws of turbulent mixing in the surface layer of the atmosphere. *Tr Akad Nauk SSSR Geophys Inst* 24(151):163–187
- Nakanishi M, Niino H (2006) An improved Mellor-Yamada level-3 model: its numerical stability and application to a regional prediction of advection fog. *Bound Layer Meteor* 119(2):397–407
- National Research Council (1992) Coastal meteorology: a review of the state of the science. The National Academies Press: Washington, DC
- Nolan DS, Zhang JA, Stern DP (2009) Evaluation of planetary boundary layer parameterizations in tropical cyclones by comparison of in situ observations and high-resolution simulations of Hurricane Isabel (2003) part I: initialization, maximum winds, and the outer-core boundary layer. *Mon Wea Rev* 137(11):3651–3674
- Nunalee CG, Basu S (2013) Mesoscale modeling of coastal low-level jets: implications for offshore wind resource estimation. *Wind Energy* 17:1199–1216
- Nunalee CG, He P, Basu S, Vorontsov MA, Fiorino ST (2014) Impact of large-scale atmospheric refractive structures on optical wave propagation. In: Proceedings of SPIE, vol 9224, pp 1–11
- Nunalee CG, He P, Basu S, Minet J, Vorontsov MA (2015) Mapping optical ray trajectories through island wake vortices. *Meteor Atmos Phys* 127(3):355–368
- Orlanski I (1975) A rational subdivision of scales for atmospheric processes. *Bull Amer Meteor Soc* 56:527–530
- Pleim JE (2007a) A combined local and nonlocal closure model for the atmospheric boundary layer part I: model description and testing. *J Appl Meteor Climatol* 46(9):1383–1395
- Pleim JE (2007b) A combined local and nonlocal closure model for the atmospheric boundary layer part II: application and evaluation in a mesoscale meteorological model. *J Appl Meteor Climatol* 46(9):1396–1409
- Puchalski J (1992) Numerical determination of ray tracing: a new method. *Appl Opt* 31(31):6789–6799
- Raftery AE, Gneiting T, Balabdaoui F, Polakowski M (2005) Using Bayesian model averaging to calibrate forecast ensembles. *Mon Wea Rev* 133(5):1155–1174

- Shin HH, Hong SY (2011) Intercomparison of planetary boundary-layer parametrizations in the WRF model for a single day from CASES-99. *Bound Layer Meteor* 139(2):261–281
- Skamarock WC, Klemp JB, Dudhia J, Gill DO, Barker DM, Duda MG, Huang XY, Wang W, Powers JG (2008) A description of the advanced research WRF version 3. In: Technical Report NCAR/TN-457+STR, National Center for Atmospheric Research
- Southwell WH (1982) Ray tracing in gradient-index media. *J Opt Soc Am* 72(7):908–911
- Steenefeld GJ, Mauritsen T, de Bruijn EIF, Vilà-Guerau de Arellano J, Svensson G, Holtslag AAM (2008) Evaluation of limited-area models for the representation of the diurnal cycle and contrasting nights in CASES-99. *J Appl Meteor Climatol* 47(3):869–887
- Stein K, Polnau E, Seiffer D (2003) IR propagation through the marine boundary layer. comparison of model and experimental data. In: Proceedings of SPIE, vol 4884, pp 84–94
- Stensrud DJ (2007) Parameterization schemes: keys to understanding numerical weather prediction models. Cambridge University Press, Cambridge
- Storm B, Dudhia J, Basu S, Swift A, Giammanco I (2009) Evaluation of the weather research and forecasting model on forecasting low-level jets: implications for wind energy. *Wind Energy* 12(1):81–90
- Sukoriansky S, Galperin B, Perov V (2005) Application of a new spectral theory of stably stratified turbulence to the atmospheric boundary layer over sea ice. *Bound Layer Meteor* 117(2):231–257
- Tapiador FJ, Tao WK, Shi JJ, Angelis CF, Martinez MA, Marcos C, Rodriguez A, Hou A (2012) A comparison of perturbed initial conditions and multiphysics ensembles in a severe weather episode in Spain. *J Appl Meteor Climatol* 51(3):489–504
- Wang C, Wilson D, Haack T, Clark P, Lean H, Marshall R (2012) Effects of initial and boundary conditions of mesoscale models on simulated atmospheric refractivity. *J Appl Meteor Climatol* 51(1):115–132
- van der Werf SY (2003) Ray tracing and refraction in the modified US1976 atmosphere. *Appl Opt* 42(3):354–366
- Xie B, Fung JC, Chan A, Lau A (2012) Evaluation of nonlocal and local planetary boundary layer schemes in the WRF model. *J Geophys Res Atmos* 117(D12):1–26
- Zhang K, Mao H, Civerolo K, Berman S, Ku JY, Rao ST, Doddridge B, Philbrick CR, Clark R (2001) Numerical investigation of boundary-layer evolution and nocturnal low-level jets: local versus non-local PBL schemes. *Environ Fluid Mech* 1(2):171–208